Structural changes in electrochemically cycled $LiMn_{0.7}Fe_{0.3}PO_4$

N.D. Trinh [a], Z.W. Ai [a], G. Liang [b], S.B. Schougaard [a]*

[a]Université du Québec à Montréal, Quebec Centre for Functional Materials, Case postale 8888 Succ. Centre-ville, Montréal, Québec, H3C 3P8, Canada

[b]Johnson Matthey Battery Materials Ltd, 280 ave. Liberté, Candiac, Québec J5R 6X1, Canada

E-mail address: schougaard.steen@uqam.ca (S.B. Schougaard)

Abstract

$Li_{(1-x)}Mn_{0.7}Fe_{0.3}PO_4$ ($0.00 \leq x \leq 1.0$) samples, obtained by electrochemical cycling, were investigated by powder X-ray diffraction (XRD) and Fourier-transform infrared spectroscopy (FTIR). The purpose of this work is to map phase transition information for samples at quasi equilibrium *i.e.* after a long relaxation time. The required high accuracy solid Li^+ content was determined by atomic emission using the standard addition method. From XRD analysis of the charging cycle samples, the phase diagram was shown to exhibit a solid solution ($0 \leq x \leq 0.42$), followed by a two phases system exhibiting both *olivine* and *heterosite* structures ($0.42 < x \leq$ ~0.91) and finally above x~0.91 the *olivine* phase is no longer detectable. The same basic pattern was found during the discharge process. Combined analysis of FTIR spectra and XRD data showed a strong correlation, where vibration bands at 690 and 600 cm^{-1} could be uniquely attributed to the *heterosite* structure.

Keywords

Lithium-ion battery; phase diagram; quasi equilibrium; solid solution; olivine; heterosite;

1. Introduction

The electric vehicles use is constantly growing, leading to a reduction of greenhouse gas emissions as a positive consequence.[1] However, to become even more attractive, this technology needs further improvement. One of the main remaining issues is the autonomy *i.e.* the distance that the electric vehicle can reach with a fully charged battery. To address this challenge, intensive efforts are made to increase the energy density.[2] As an example, lithium iron phosphate, $LiFePO_4$, provides a theoretical energy density of ~586 Wh kg^{-1} *vs* a lithium

anode. This however may be insufficient for long range transportation.[3] One improvement strategy is partial substitution of the Fe^{2+}/Fe^{3+} redox couple by another 3*d* transition metal with a higher redox potential.[4] In this context $LiMn_yFe_{1-y}PO_4$ represents a promising candidate because of the possible combination of the high rate electrochemical performance of $LiFePO_4$ and the higher operational voltage from the Mn^{2+}/Mn^{3+} redox couple (4.10 V *vs* Li/Li^+).[5] However, substituted materials necessary imply modifications in the intrinsic properties, which leads to different phase transformation compared to pure $LiFePO_4$.[6]

The equilibrium reactions of delithiation and relithiation of $LiFePO_4$ occurs *via* a two phase mechanism. The two phases are described as Li-rich (*olivine*) and Li-poor (*heterosite*), with solid solutions formed close to both end members of the Li_xFePO_4 phase diagram.[7-8] According to the Domino-cascade model, the Li^+ diffusion only occurs along the *b* axis of the unit cell, while the boundary moves along the *a* axis.[9] In contrast to this model, a non-equilibrium solid solution mechanism is possible, demonstrated by both theoretical calculations and experimental observations.[10-12] This latter mechanism is kinetically favorable because the lithium ion is free to move inside the structure, avoiding both lattice strain at the $LiFePO_4/FePO_4$ interface and the formation of nucleation sites.[13] In comparison, the $LiMn_yFe_{1-y}PO_4$ dynamic electrochemical response and proposed mechanisms have a strong dependence on Mn/Fe ratio.[14-20] Consequently, the target here is *ex situ* X-ray diffraction (XRD) of a quasi equilibrium state *i.e.* after a long time relaxation period, as a point of comparison for dynamic data. As such, we expand on the work of Yamada *et al.* who performed structural analysis of chemically delithiated $LiMn_yFe_{1-y}PO_4$ compositions.[21-22] We here use an electrochemical technique to eliminate possible Mn dissolution by oxidation using NO_2^+, and by adding Fourier-transform infrared spectroscopy (FTIR) to examine the local structure evolution.

2. Experimental section

2.1. Material characterization

Carbon coated $LiMn_{0.7}Fe_{0.3}PO_4$ (LMFP) powder was provided by Johnson Matthey Battery Materials Ltd (Candiac). The carbon content was determined by CHNS elemental analysis (EAS1108, Fisons Instruments). Transmission electron microscopy (TEM) was performed with a JEOL JEM-2100F and an acceleration voltage of 200 keV. TEM samples were prepared

by suspending powders in methanol using an ultrasonic bath, before deposition onto a carbon grid. The powder was characterized by *ex situ* X-ray diffraction using a Phillips X'Pert Pro diffractometer with Cu K_α radiation (1.5418 Å). The current and voltage were 40 mA and 50 kV respectively with a step size of 0.015 ° s^{-1} in the 2θ range of 15-75 °. 10 % m/m silicon powder 1-5 µm (Alfa Aesar 99.5 %) was mixed into the sample, as an internal standard. Rietveld refinement was performed Fullprof 3.2 software.[23] Fourier-transform infrared spectroscopy (FTIR) was performed on a Nexus 670 FTIR Nicolet: A mixture of ~1 mg of the material and 300 mg of KBr (Fischer Scientific) was ground to a homogeneous powder and pressed to form a pellet of ~1 mm thickness. The spectral range of 1500-300 cm^{-1} was probed with a total of 32 scans combined for each spectrum. The lithium content in the solid samples was determined by dissolving 8-10 mg of the electrode powder in 20 mL of boiling concentrated nitric acid (Caledon). The mixture was allowed to react for one hour or until complete dissolution. The solution was passed through a 20 µm filter to remove residual carbon particles. The sample was diluted to fit within a calibration curve spanning concentrations between 0.1 to 0.6 ppm of Li^+ (Alfa Aesar standard solution). The acquisition was performed using a Varian SpectrAA 220 FS at 670.8 nm wavelength. Standard addition method was used to quantify the lithium concentration in the sample mainly to avoid possible interference from the electrode matrix. Inductive coupled plasma spectroscopy (ICP, Thermo 6500 Dual View) is used to quantify the iron, manganese and phosphorous contents of the starting material at 259.9 nm, 257.6 nm and 177.4 nm respectively. The sample was diluted to fit in the calibration curve of the respective element spanning from 0.5 to 5 ppm for the Fe, Mn and P elements, in a 5 % HNO_3 medium (SpectraPure, Fisher Alfa Aesar and standard solutions respectively).

2.2. Electrochemistry procedure

The electrodes were made by preparing a slurry composed of 80 % of active material, 12 % of acetylene black (MTI Corp.) and 8 % of PVDF (Kynar KF Polymer W#1100) in N-methylpyrrolidone (NMP, Alfa Aesar 99.5 %). The mixture was stirred using a roller mill for 24 hours to obtain a uniform suspension before casting on an aluminum current collector (MTI Corp.) with a film applicator (BYK-Gardner USA) adjusted to 90 µm. The composite electrode was dried at 60°C at atmospheric pressure for two hours and then under vacuum at 60°C for 24 hours. From the obtained electrode, rectangles of specific dimension (6 cm × 3.5 cm) were cut. The upper portion of the composite was scraped from the electrode (2 cm), freeing space for electrical connection. The geometric area electrodes immerged in the electrolyte was estimated

at 14 cm^2. The average thickness (~70 µm) of the electrodes was measured by a Mitutoyo 7326S thickness gage, for an active material loading of 1.1 to 1.4 mg cm^{-2}.

The electrochemical delithiation/relithiation was performed in a home made three electrodes cell using a Bio-Logic VMP3 potentiostat. The electrochemical cell was composed of an inner fritted container accommodating the reference, Li foil (Alfa Aesar 99.95%) soaked in electrolyte behind Vycor frit, and working electrodes in 0.5 M $LiClO_4$ (Alfa Aesar 99.8%) in propylene carbonate (Sigma Aldrich 99.9%). A Li foil (1.5 cm × 6 cm), placed directly underneath the fritted inner container in the outer beaker served as the counter electrode. All the experiments were performed in an argon filled gloves box.

For the charging process, a constant current at C/10 was imposed with a 4.35 V *vs* Li/Li^+ upper cut-off. Charging was carried out for times varying between 30 minutes to 10 hours, to obtain various Li^+ contents in $Li_{(1-x)}Mn_{0.7}Fe_{0.3}PO_4$ ($0.00 < x \leq 1.0$). To obtain high values of x, a constant potential at 4.35 V *v*s Li/Li^+ was imposed. A similar procedure was used to obtain samples from the discharge cycle, using a C/10 constant current. Finally, the working electrode was removed from the reactional media and rinsed with anhydrous acetonitrile (Sigma Alrich 99.9%) in the glove box. The electrodes were dried at 60°C under vacuum for 24 hours before further use. The electrode composition was scratched off from the current collector and ground to obtain a uniform powder.

To verify the electrochemical activity of the active material, CR2032-type coin cells were assembled using metallic lithium (Alfa Aesar 99.9%) as the negative electrode, and a disk electrode (d = 14 mm) cut from a rectangle electrodes detailed above as the positive electrode. The electrolyte was 1 M $LiPF_6$ in a 1:1 ethylene carbonate (EC) and dimethyl carbonate (DMC) mixture (Novalyte Technologies) and porous polypropylene (Celgard 2500) was used as the separator. The cells were assembled in an argon atmosphere glove box. Electrochemical testing was performed by galvanostatic cycling using a C/20 current between 2.2-4.3 V *vs* Li/Li^+ at room temperature, and a BST8-MA (MTI ltd.) battery analyzer. An open circuit rest period was imposed during one hour at charge reversal.

3. Results and discussion

3.1. Starting material $LiMn_{0.7}Fe_{0.3}PO_4$

TEM micrograph showed the samples to be composed of agglomerates of semi-spherical particles with diameter of ~100 nm (Fig. 1a). High resolution TEM micrograph (Fig. 1b) demonstrated well-defined lattice planes inside the particle and a carbon coating thickness of ~3-4 nm. Elemental analysis showed a carbon content of 1.18 m/m%.

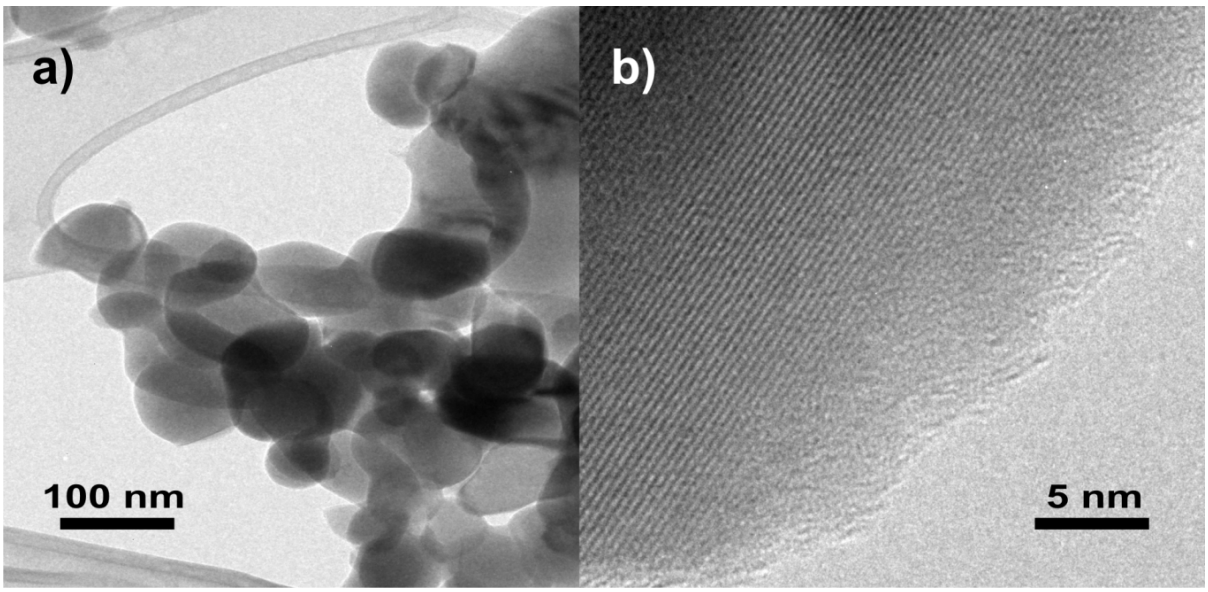

Figure 1. a) TEM micrograph showing the morphology and particle size and b) HRTEM micrograph of a single particle showing the thickness of the carbon layer and the lattice fringes.

The crystalline structure was confirmed by powder X-ray diffraction (Fig. 2). The reflections are indexed in the *orthorhombic* crystal system with space group *Pnma*.[24] Rietveld refinement lattice parameters were a = 10.4116 (3) Å, b = 6.0717 (2) Å, c = 4.7268 (1) Å yielding a unit cell volume of 298.81 (2) $Å^3$, similar to previous works.[24] More importantly, there were no unassigned peaks, thus confirming the absence of crystalline impurities in the starting material. Finally, the Li/P (1.00 ± 0.03), Fe/P (0.31 ± 0.01) and Mn/P (0.69 ± 0.02) ratios obtained by atomic emission and inductive coupled plasma spectrometry, were consistent with the $LiMn_{0.7}Fe_{0.3}PO_4$ stoichiometry.

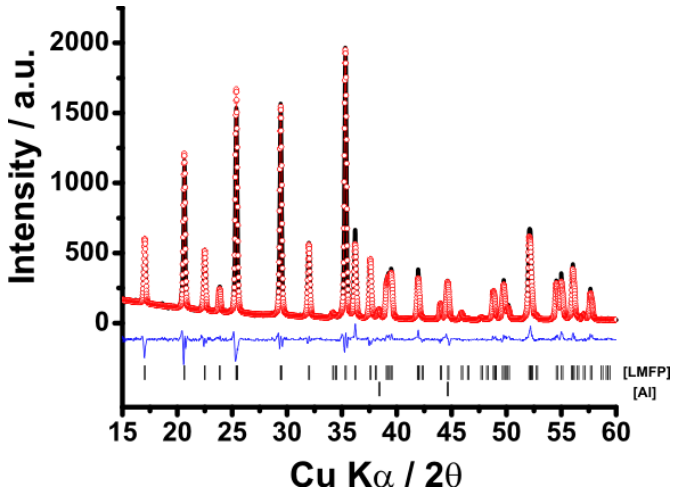

Figure 2. Diffractogramm and Rietveld refinement of the starting material $LiMn_{0.7}Fe_{0.3}PO_4$. Peak positions derived from [24] are included under the label [LMFP], Al peaks originate from the sample holder.

The electrochemical response (Fig. 3a), showed two plateaus; one at 3.56 V *vs* Li/Li^+ attributed to the Fe^{2+}/Fe^{3+} redox couple and a second at 4.15 V *vs* Li/Li^+ attributed to Mn^{2+}/Mn^{3+}.[25] The discharge capacity was ~139 mAh g^{-1} at a current rate of C/20 and with a coulombic efficiency above 99 %, remaining approximately constant during 30 cycles at room temperature (Fig. 3b). There are no changes observed in the voltage profiles as the electrochemical cycling progressed.

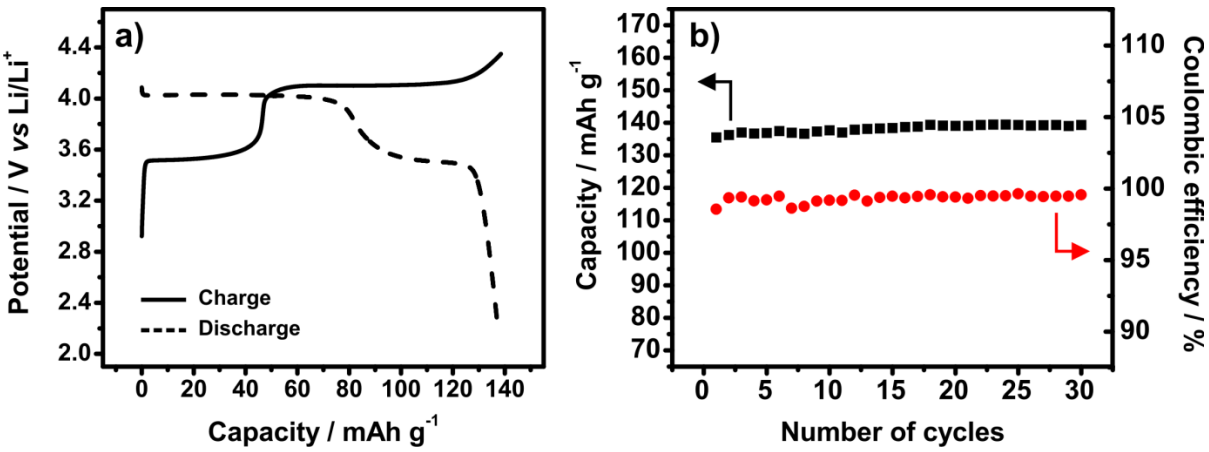

Figure 3. a) Voltage profile for galvanostatic charge and discharge at C/20 current rate demonstrating plateaus for the Fe^{2+}/Fe^{3+} and Mn^{2+}/Mn^{3+} redox couples and b) discharge capacity (black square) and coulombic efficiency (red circle) at C/20 current rate of the C-$LiMn_{0.7}Fe_{0.3}PO_4$ at room temperature.

3.2. Structural characterization

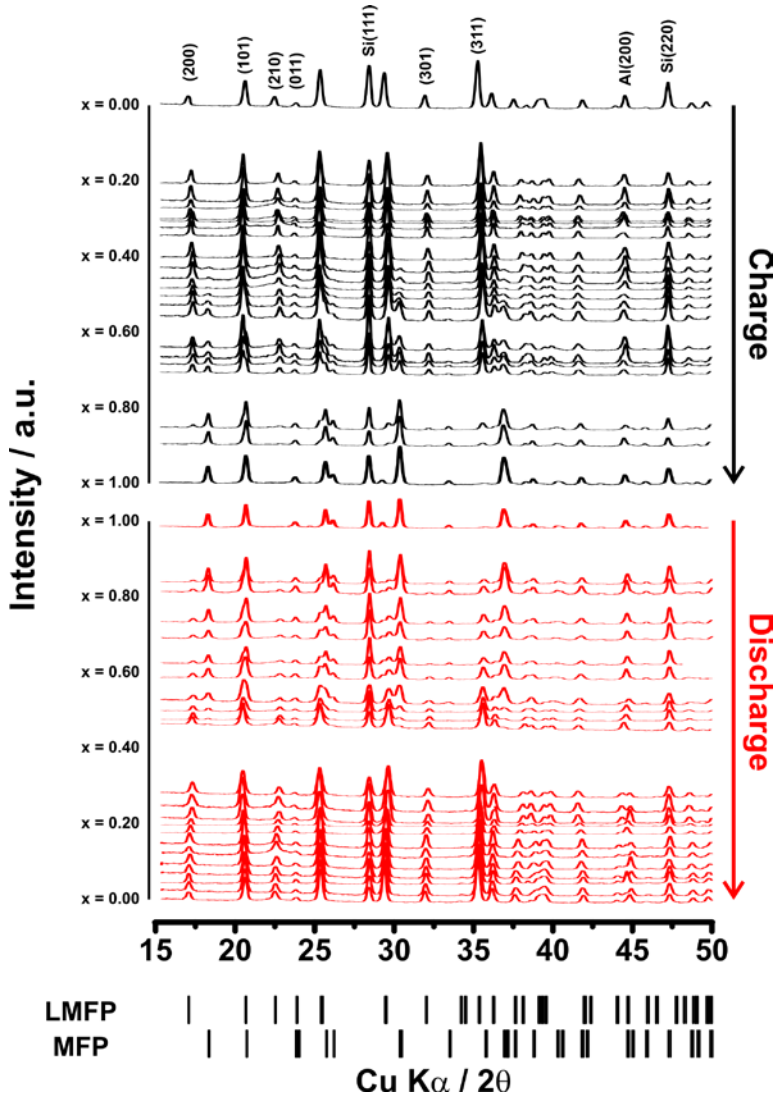

Figure 4. XRD patterns collected at different x values in $Li_{(1-x)}Mn_{0.7}Fe_{0.3}PO_4$ obtained after electrochemical charge (black) and discharge (red) process. LMFP and MFP reference peak positions are derived from [24].

First cycle $Li_{(1-x)}Mn_{0.7}Fe_{0.3}PO_4$ XRD patterns (Fig. 4), show the *olivin*e starting material delithiate initially *via* a solid solution mechanism, *i.e.* monotonic shift of diffraction peaks most clearly seen for the (200) reflection and no evidence of a second crystalline phase. Beyond, x ~0.42 delithiation leads to phase separation into an *olivine* and *heterosite* phase. This is particularly evident from the area of the (200) peak of the *olivine* (17.3°) which decreases while the *heterosite* (18.3°) increases proportionally until a single *heterosite* $Mn_{0.7}Fe_{0.3}PO_4$ phase is observed at x = 1.0 (Fig. 5). During discharge, the first diffractogramm only shows the *heterosite* phase at x = 0.97, which could be indicative of a narrow solid solution region at the

end member of the phase diagram, as found in the Li_xFePO_4 system.[8] However at such low phase concentrations, and consequently low signal to noise ratio, such an assignment cannot be made reliably. Continuing relithiation shows that for x = 0.86 two phases continues to exist, and the area of the reflection (200) of the Li-rich phase continuously increases at the expense of the Li-poor phase until x ~0.50 (Fig. 5). As the relithiation progresses from x = 0.50 to 0.00, the diffractogramms only show the *olivine* structure, and a (200) shift consistent with a solid solution. Finally, peak positions return to their initial values at x = 0.00.

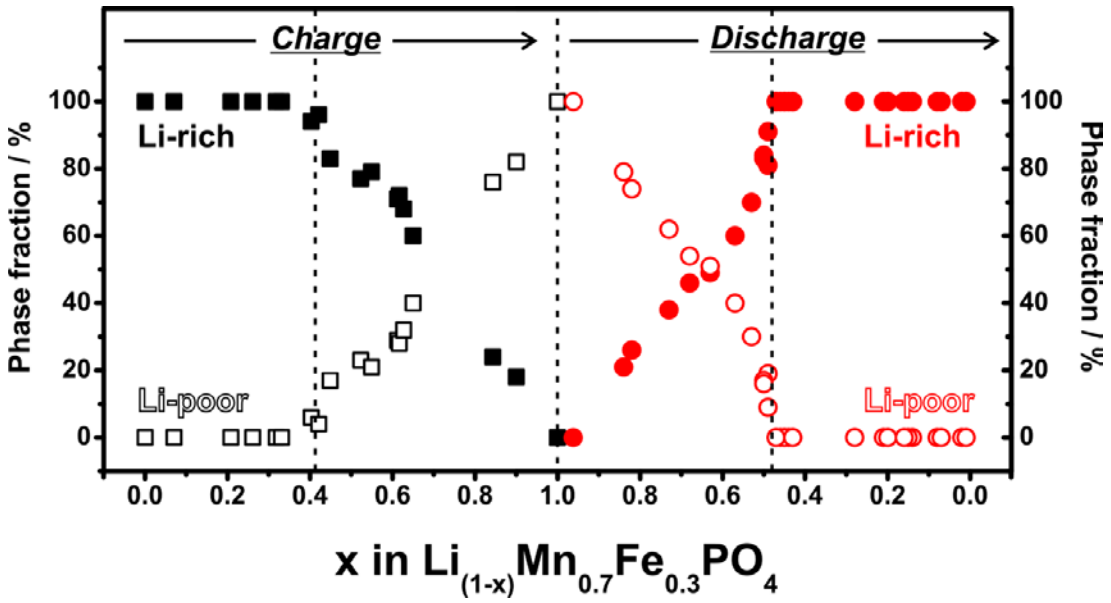

Figure 5. Variation of the phase fraction as determine by Rietvelt refinement of the Li-rich (charge-black square, discharge-red circle) and Li-poor (charge-unfilled black square, discharge-unfilled red circle).

The unit cell lattice parameters of the *olivine* structure as a function of Li^+ content indicates that as delithiation occurs, the *a* and *b* axis contracts while the *c* axis expands until reaching x = 0.42 in $Li_{(1-x)}Mn_{0.7}Fe_{0.3}PO_4$ (Fig. 6). The *a* and *c* unitcell axis then remain stable upon further delithiation ($0.42 < x \leq 1.00$) as expected for the two phase system. However, the lattice parameter *b* continues to decrease. The source of contraction is not clear yet, but residual strain is a possibility. The unit cell volume of the *olivine* decreases during solid solution delithiation ($0.0 \leq x \leq 0.42$) following Vegard's law consistent with the smaller ionic radius of both oxidized Fe^{3+} (0.65 Å) and Mn^{3+} (0.65 Å) compared to Fe^{3+} (0.75 Å) and Mn^{2+} (0.83 Å) as well as introduction of Li vacancies.[26] Unfortunately, the scatter of the data does not allow a detailed volume analysis. The lattice parameters for the *heterosite* structure remain stable throughout the reaction. The lattice parameters of $Mn_{0.7}Fe_{0.3}PO_4$ are *a* = 9.6876 (4) Å, *b* =

5.8764 (2) Å, c = 4.7852 (2) Å and the unit cell volume is 272.41 (2) Å^3, all of which are in concordance with previously published results.[27] Upon completion of the discharge, the lattice parameters have returned to their initial values.

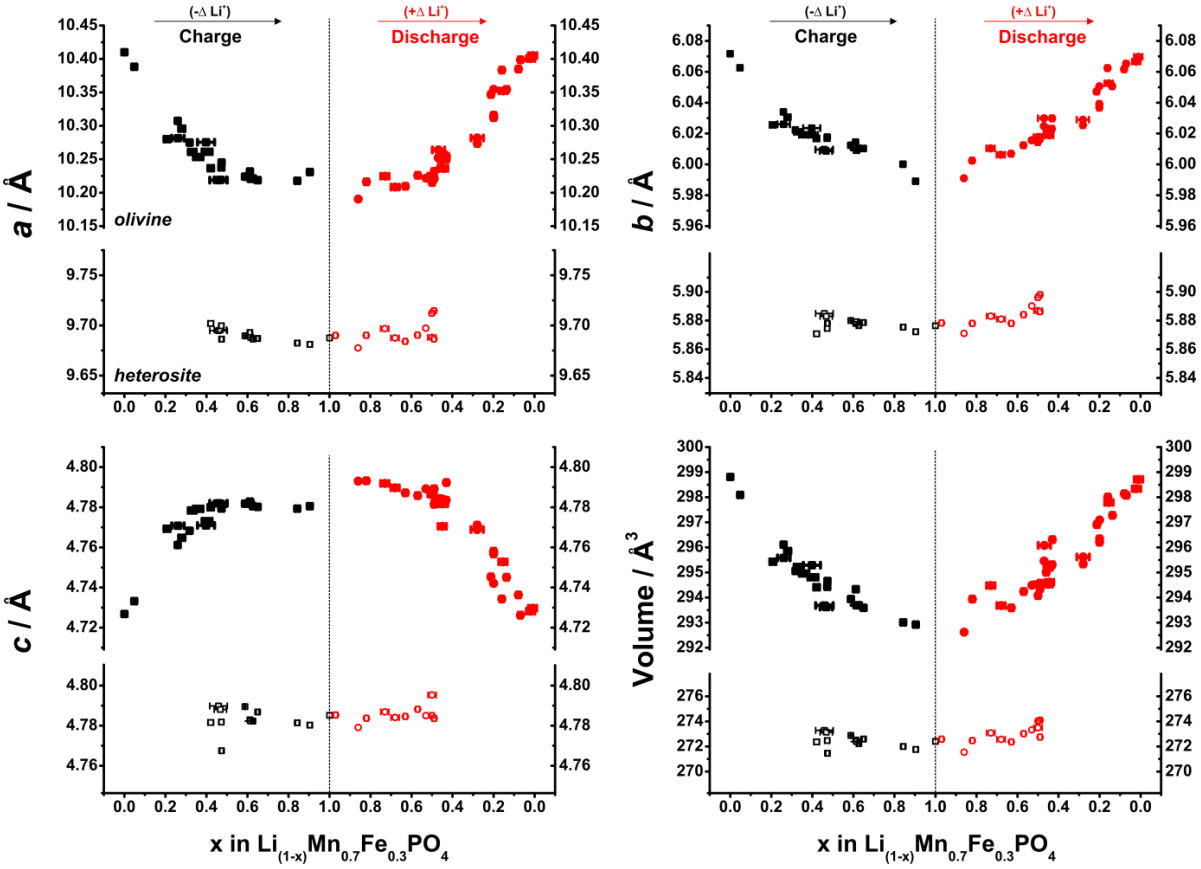

Figure 6. Evolution of the unit cell parameters of the *orthorhombic* space group *Pnma* (*a*, *b*, *c* and volume) obtained at different x values in $Li_{(1-x)}Mn_{0.7}Fe_{0.3}PO_4$ after electrochemical charge and/or discharge.

3.3. Local characterization with FTIR

The FTIR spectroscopy was used to locally probe the chemical bonds of both crystalline and possible amorphous phases. The FTIR spectra are reported for the charge and discharge process for $Li_{(1-x)}Mn_{0.7}Fe_{0.3}PO_4$ in Fig. 7. The spectrum of the starting material $LiMn_{0.7}Fe_{0.3}PO_4$ shows wider vibration bands in the 1300 to 450 cm^{-1} range comparable to pure $LiFePO_4$ and $LiMnPO_4$, caused by the mixture of both transition metals affecting the P-O bands.[28-29] These bands are assigned into two domains. The domain at 1300-800 cm^{-1} is assigned to the ν_3 antisymmetric (1100-1000 cm^{-1}) and the ν_1 symmetric (950 cm^{-1}) PO_4 stretching. The lower wavenumbers domain (750-450 cm^{-1}) related to a mixture of symmetric and antisymmetric bending mode at 700-600 cm^{-1}.[29] During the delithiation, the spectral features become increasingly smeared,

consistent with many distinct local environments and/or disorder. Close examination of the 300-1200 cm^{-1} range, shows that the 1237 cm^{-1} peak (ν_3) used to identify the *heterosite* structure in the Li_xFePO_4 system is not present. In the spectra published by Norberg *et al*. of $Li_{0.15}MnPO_4$, this peak found at 1264 cm^{-1} is very weak.

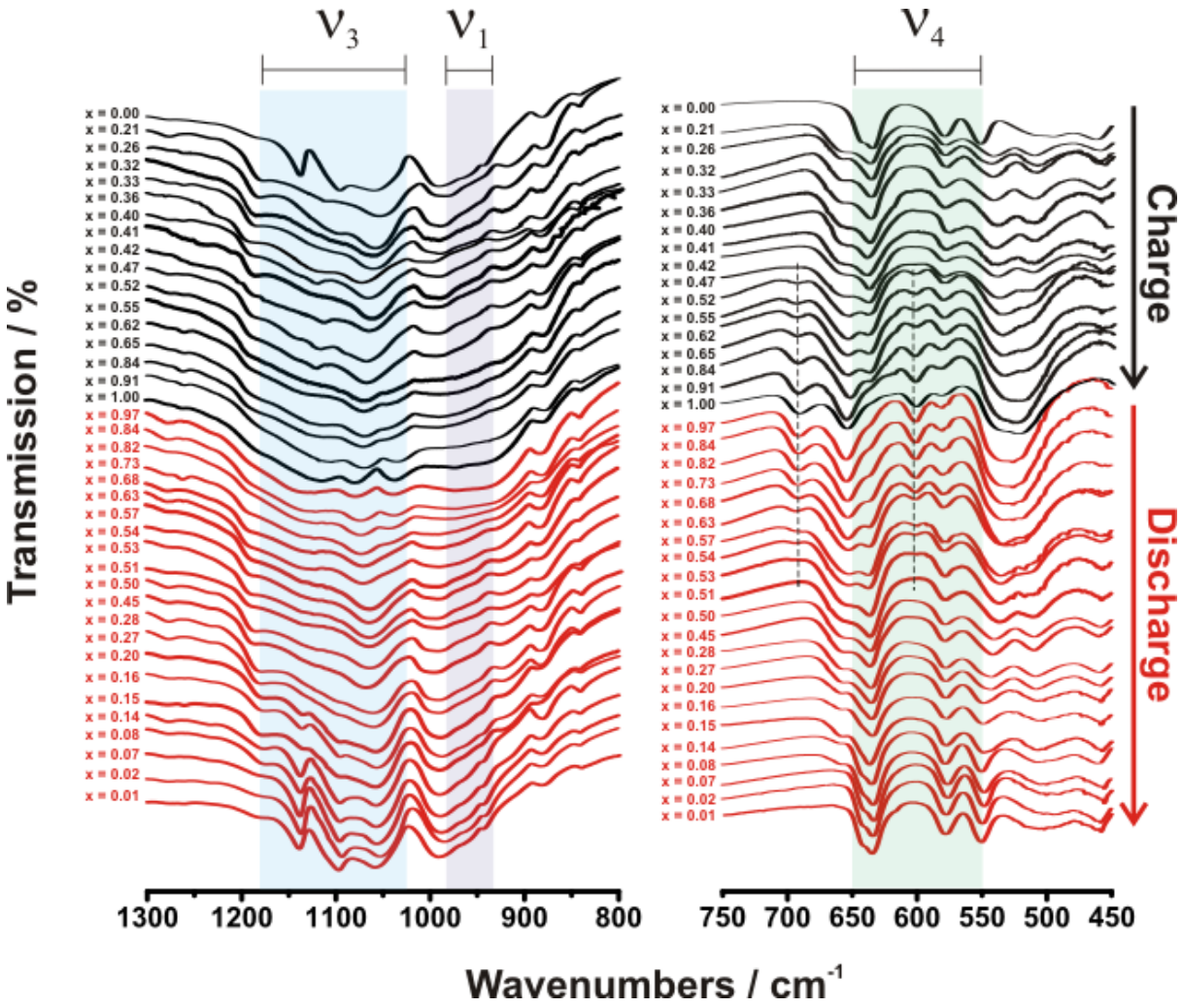

Figure 7. FTIR spectra of $Li_{(1-x)}Mn_{0.7}Fe_{0.3}PO_4$ obtained after electrochemical charge and/or discharge. 1300 to 800 cm^{-1} (left) and 750 to 450 cm^{-1} (right).

At lower wavenumbers, a new peak appears at 660 cm^{-1} attributed to phosphate close to a M^{3+} (M = Fe, Mn) and the associated Li vacancy site, unlike the peak at 640 cm^{-1}, which is attributed to the phosphate close to M^{2+} and filled Li sites.[29] The intensity trend of these peaks does not appear to be affected by the transition from a single phase to a two-phase system or from the transition from Fe to Mn oxidation at x = 0.30, which could have been expected due to the radii difference of the reduced relative to the oxidized form of Mn (28%) compared to Fe (20%). The peak at 575 cm^{-1} is unaffected by Li^+ composition, and therefore have no diagnostic

value. The two peaks at 550 and 500 cm^{-1} converge to form a single broad peak at 525 cm^{-1}, but the trend is not affected at x = 0.30 (Fe to Mn transition) or x = 0.42 (phase separation). In contrast, two new peaks at 690 and 600 cm^{-1} appeared specifically with the phase separation *i.e.* $0.42 \leq x \leq 1.0$. The peaks increase with the delithiation and can thus be attributed to the *heterosite* phase. The discharge process yields a reversible evolution of the vibration peaks which return the spectra to its initial state, without any indication of new peaks. The FTIR spectra did not exhibit any distinct features as the active site changes from Fe to Mn during oxidation. Moreover, we found no observations in the infrared data inconsistent with the X-ray diffraction data *i.e.* bands that are unique to the *heterosite* structure were identified only when this phase was found in the X-ray data.

3.4 Phase transition mechanisms

3.4.1 Comparison with previous studies

Several studies concerning the structural behavior have been performed on similar materials. Perea *et al.* performed *in situ* XRD on $Li_{(1-x)}Mn_{0.75}Fe_{0.25}PO_4$ and observed similar structural behaviour as our experiments in term of crystalline structures.[18] Nevertheless there is significant difference compared to the present study, as they stated the appearance of the second phase occurs at exactly x = 0.25, commensurate with the transition from Fe to Mn oxidation. Similarly, the *ex situ* study by Yamada *et al.*[21] using chemical delithiation and relithiation showed $Li_{(1-x)}Mn_{0.7}Fe_{0.3}PO_4$ phase separation to occur at x = 0.30, in accord with active redox center shift from Fe to Mn. In our study, however, an extended solid solution domain of $0.00 < x \leq 0.42$ for the charge and $0.00 < x \leq 0.50$ for the discharge was established, *i.e.* a non-negligible amount of Mn^{3+} (up to 17%) was required before the phase separation was initiated in $Li_xMn_{0.7}Fe_{0.3}PO_4$. Moreover, a phase transition hysteresis relative to x was found in our study, which may be related to the possible Jahn-Teller distortion of Mn^{+3}. Briefly, the only charge and element combination in the Mn-Fe system that is susceptible to Jahn-Teller distortion is Mn^{+3}. It is therefore possible that the bond rearrangement for this ion upon phase separation is significantly more difficult to obtain, and the Jahn-Teller distortion is therefore a likely candidate for the origin of the hysteresis.

3.4.2 Extended solid solution

From the experimental data, the phase transition of $LiMn_{0.7}Fe_{0.3}PO_4$ is mainly described by two distinct domains. The first domain ($0.00 < x \leq 0.42$) is described as an extended solid solution

(Fig. 4). Interestingly, the solid solution region is larger compared to pure $LiFePO_4$ or $LiMnPO_4$ structures ($0.00 < x \leq \sim 0.05$). During the delithiation, the oxidation of Fe^{2+}/Fe^{3+} redox centers occurs first because of their lower redox potential. Since, the Fe sites are distributed throughout the structure, the oxidation of the former sites leads to a solid solution due to the cost of Li^+ rearrangement required for phase separation. Indeed the lithium ions must remain in close proximity to the M^{2+} sites due to electrostatic energy considerations.[30] Therefore to obtain a significant Li concentration gradient, *i.e.* a phase separation, requires that lithium be transferred from a site close to a Mn^{2+} to a site in proximity to Fe^{3+}, which is only possible if an electron follows. The net effect would therefore be a Mn^{2+} to Mn^{3+} and Fe^{2+} to Fe^{3+} redox process, which comes at a 0.7 V ≈ 67.5 kJ mol^{-1} penalty.

Upon further delithiation ($0.30 \leq x$) Mn^{3+} is formed, however in our samples ~17% of Mn^{2+} must oxidized before phase separation takes place, *i.e.* there is no correlation between the transition for Fe to Mn oxidation and the formation of the second phase. The possible explaination for this opservation is detailed in the following.

The process of separating the solid solution into two phases, is driven by the bonding enthalpy, *i.e.* on an average bond length optimization. Working agents phase separation is the entropy reduction associated with converting the solid solution into two phases. Together, the entropy and enthalpy contributions leads to a free energy that scales with the volume of the new phase. Conversely, the strain energy originating from the interphase between the new phases scales with the area. Accordingly, phase separation is thermodynamically favorable only once a critical number of unit cells has been delithiated. Since the ionic size of Mn^{3+} and Fe^{3+} is identical, the *heterosite* phase unitcell should be similar to the one found in $LiFePO_4$, which confirmed experimentally ($FePO_4$: 272Å^3[3]; $Fe_{0.3}Mn_{0.7}PO_4$:272 Å^3). However, the unitcell volume difference between the *olivine* phase at x=0.30 and $LiFePO_4$ is considerable (~295Å^3 *vs* 292Å^3) due to the large Mn^{2+} ionic size *vs* Fe^{2+}. Since a second phase is not detected at x=0.30, it follows that surface strain energy associated with forming the *hetrosite* phase would be larger in the FeMn *vs* the Fe system, and apparently insurmountable. However once x=0.47 is reached during delithiation the second phase starts to form. This process is favored by two factors, 1) the unitcell size of the solid solution *olivine* phase has contracted to ~293 Å^3 and 2) the number of unicells that contains only +3 ions has significantly increased. The second factor may also be important relative to relaxing the lattice around Mn^{+3} to accommodate the Jahn-Teller distortion.

4. Conclusions

In this paper, we report a detailed study of the structure and the phase transitions in $Li_{(1-x)}Mn_{0.7}Fe_{0.3}PO_4$ from a quasi equilibrium point of view, *i.e.* after a long period of relaxation. A systematic structural investigation at different Li^+ content was performed from samples obtained during the first electrochemical cycle. From the crystallographic data, it was possible to highlight a transformation mechanism based on the phase fraction evolution, the unit cell parameters variation. Two main regions are involved; the initial release of Li^+ is governed by a solid solution until x = 0.42 in $Li_{(1-x)}Mn_{0.7}Fe_{0.3}PO_4$ during the charge. The second region involves a two-phase mechanism at least until x~0.91, where after the Li-rich *olivine* phase is no longer detectable. During the discharge, reinsertion of Li^+ is shown to lead to two phases at least from x=0.84 to x = 0.50, followed by a solid solution reaction. From the FTIR spectra, we found that P-O vibration bands are influenced by the Li^+ content in the solid and an interesting set of vibration bands at 600 and 690 cm^{-1} appears with the formation of the *heterosite* Li-poor structure were identified.

5. References

[1] E. Graham-Rowe, B. Gardner, C. Abraham, S. Skippon, H. Dittmar, R. Hutchins, J. Stannard, *Transportation Research Part A: Policy and Practice* **46** (2012) (1) 140.
[2] A. Poullikkas, *Renewable and Sustainable Energy Reviews* **41** (2015) 1277.
[3] A.K. Padhi, K.S. Nanjundaswamy, J.B. Goodenough, *Journal of The Electrochemical Society* **144** (1997) (4) 1188.
[4] K.-W. Nam, W.-S. Yoon, K. Zaghib, K. Yoon Chung, X.-Q. Yang, *Electrochemistry Communications* **11** (2009) (10) 2023.
[5] S.K. Martha, J. Grinblat, O. Haik, E. Zinigrad, T. Drezen, J.H. Miners, I. Exnar, A. Kay, B. Markovsky, D. Aurbach, *Angewandte Chemie International Edition* **48** (2009) (45) 8559.
[6] R. Malik, F. Zhou, G. Ceder, *Physical Review B* **79** (2009) 214201.
[7] L. Laffont, C. Delacourt, P. Gibot, M.Y. Wu, P. Kooyman, C. Masquelier, J.M. Tarascon, *Chemistry of Materials* **18** (2006) (23) 5520.
[8] J.L. Dodd, R. Yazami, B. Fultz, *Electrochemical and Solid-State Letters* **9** (2006) (3) A151.
[9] C. Delmas, M. Maccario, L. Croguennec, F. Le Cras, F. Weill, *Nat Mater* **7** (2008) (8) 665.
[10] R. Malik, F. Zhou, G. Ceder, *Nat Mater* **10** (2011) (8) 587.
[11] P. Gibot, M. Casas-Cabanas, L. Laffont, S. Levasseur, P. Carlach, S. Hamelet, J.-M. Tarascon, C. Masquelier, *Nature Materials* **7** (2008) (9) 741.
[12] C. Delacourt, P. Poizot, J.-M. Tarascon, C. Masquelier, *Nat Mater* **4** (2005) (3) 254.
[13] A. Khawam, D.R. Flanagan, *The Journal of Physical Chemistry B* **110** (2006) (35) 17315.
[14] I. Bezza, M. Kaus, R. Heinzmann, M. Yavuz, M. Knapp, S. Mangold, S. Doyle, C.P. Grey, H. Ehrenberg, S. Indris, I. Saadoune, *The Journal of Physical Chemistry C* **119** (2015) (17) 9016.

[15] W. Huang, S. Tao, J. Zhou, C. Si, X. Chen, W. Huang, C. Jin, W. Chu, L. Song, Z. Wu, *The Journal of Physical Chemistry C* **118** (2014) (2) 796.
[16] J. Hong, F. Wang, X. Wang, J. Graetz, *Journal of Power Sources* **196** (2011) (7) 3659.
[17] D.B. Ravnsbæk, K. Xiang, W. Xing, O.J. Borkiewicz, K.M. Wiaderek, P. Gionet, K.W. Chapman, P.J. Chupas, Y.M. Chiang, *Nano Letters* **14** (2014) (3) 1484.
[18] A. Perea, M.T. Sougrati, C.M. Ionica-Bousquet, B. Fraisse, C. Tessier, L. Aldon, J.-C. Jumas, *RSC Advances* **2** (2012) (25) 9517.
[19] A. Perea, M.T. Sougrati, C.M. Ionica-Bousquet, B. Fraisse, C. Tessier, L. Aldon, J.-C. Jumas, *RSC Advances* **2** (2012) (5) 2080.
[20] N.N. Bramnik, K.G. Bramnik, K. Nikolowski, M. Hinterstein, C. Baehtz, H. Ehrenberg, *Electrochemical and Solid-State Letters* **8** (2005) (8) A379.
[21] A. Yamada, Y. Kudo, K.-Y. Liu, *Journal of The Electrochemical Society* **148** (2001) (10) A1153.
[22] A. Yamada, Y. Kudo, K.-Y. Liu, *Journal of The Electrochemical Society* **148** (2001) (7) A747.
[23] H. Rietveld, *Journal of Applied Crystallography* **2** (1969) (2) 65.
[24] J. Yao, S. Bewlay, K. Konstantionv, V.A. Drozd, R.S. Liu, X.L. Wang, H.K. Liu, G.X. Wang, *Journal of Alloys and Compounds* **425** (2006) (1–2) 362.
[25] G. Kobayashi, A. Yamada, S.-i. Nishimura, R. Kanno, Y. Kobayashi, S. Seki, Y. Ohno, H. Miyashiro, *Journal of Power Sources* **189** (2009) (1) 397.
[26] R. Shannon, *Acta Crystallographica Section A* **32** (1976) (5) 751.
[27] M. Kopec, A. Yamada, G. Kobayashi, S. Nishimura, R. Kanno, A. Mauger, F. Gendron, C.M. Julien, *Journal of Power Sources* **189** (2009) (2) 1154.
[28] C.M. Burba, R. Frech, *Journal of The Electrochemical Society* **151** (2004) (7) A1032.
[29] N.S. Norberg, R. Kostecki, *Electrochimica Acta* **56** (2011) (25) 9168.
[30] M.Z. Bazant, *Accounts of Chemical Research* **46** (2013) (5) 1144.